PHYSICAL REVIEW E **69**, 036407 (2004)

Fast ion acceleration in ultraintense laser interactions with an overdense plasma

H. Habara,[1,*] R. Kodama,[1] Y. Sentoku,[1] N. Izumi,[1,†] Y. Kitagawa,[1] K. A. Tanaka,[1,2] K. Mima,[1] and T. Yamanaka[1]
[1]*Institute of Laser Engineering, Osaka University, Suita, 565-0871 Osaka, Japan*
[2]*Faculty of Engineering, Osaka University, Suita, 565-0871 Osaka, Japan*

(Received 2 May 2003; revised manuscript received 7 November 2003; published 24 March 2004)

In order to study the ion acceleration processes in ultraintense laser-plasma interactions with solid targets, neutron spectra from deuteron-deuteron (D-D) nuclear reactions were measured. Spectra were obtained when (50–100 TW, 0.5–1 ps) laser light irradiated obliquely incident deuterated plastic targets as a function of laser polarization, intensity, and density scale length of the preformed plasma. The experimental data are compared with three-dimensional Monte Carlo simulations. The results indicate that the ion momentum distribution is collimated and directed into the bulk of the target to the target normal direction with an energy that is linearly proportional to the laser intensity. The distribution of the accelerated ions was observed to change from isotropic to anisotropic with laser prepulse intensity. All the results indicate that the ion acceleration is dominated by an electrostatic field generated from a charge displacement of the hot electrons at the target surface.

DOI: 10.1103/PhysRevE.69.036407 PACS number(s): 52.38.Kd, 52.25.Tx, 52.38.−r

I. INTRODUCTION

The emission of energetic particles in high power laser-plasma interactions are vitally important not only in fast ignitor scheme [1] in inertial conferment fusion research but also for many applications in nuclear physics [2], astrophysics [3], and even in biological and medical application that require bright particle sources.

In recent studies, energetic ions with energies of over MeV range have been observed in interaction of intense laser light with solid targets [4–6], gas jets [7], and clusters [8]. At the rear side of solid target, it is now accepted that ions are accelerated by the electrostatic field due to the sheath potential between the escaping electrons and the ions [9,10]. It is also understood that ions can be accelerated into the target from the front surface [6,11], but these acceleration mechanisms have not been understood in detail due to the complexity of the processes involved. The ions are accelerated by electric fields set up by the electrons since the ions are too heavy to be directly accelerated by laser field efficiently to energies over the MeV range with focused intensities below $10^{22}\ \mathrm{W\,cm^{-2}}\ \mu\mathrm{m}^2$. Several possibilities have been investigated theoretically such as direct Coulomb potential between electrons and ions [12], Coulomb expansion [8] (as in clusters), the static field acceleration that takes the same form as the rear acceleration [9,10], and shock acceleration [13] by a solitary wave.

To understand the dominant mechanism(s), it might be helpful to measure the energy and angular distribution of the accelerated ions. There are several ways to detect the accelerated ions: Direct observation of the energetic ions are usually carried out using Thomson parabola and a track detector such as CR39 [4,6]. Direct measurement of ions from the plasma some distance from the target necessarily involves an uncertainty in the ion momentum distribution due to the possibility that the strong electric and magnetic field around the target affects the distributions that is measured there. On the other hand, indirect measurements, such as neutrons generated through nuclear reactions among the accelerated ions in a beam-type–fusion-type process avoid these problems altogether but, of course, are more difficult to measure and interpret accurately [14–16].

In previous papers, we presented neutron spectroscopic measurements that supported the ion acceleration of ‘‘hole-boring model’’ for normal incidence [11] and the static field model for oblique incidence [17]. Here, a comprehensive study of the ion acceleration processes from the front surface is presented, a study that includes the laser polarization, intensity, and prepulse dependence of the processes. The momentum distribution of ions are extracted by neutron spectra detected simultaneously from several viewing directions using a three-dimensional Monte Carlo calculation to fit the calculated spectra to the experimental results. All the results indicate that the ion acceleration is generated by an electrostatic field induced by the strong laser field.

II. EXPERIMENTAL SETUP

These laser-plasma interaction experiments use the 30 and 100 TW short pulse glass laser systems Gekko M-II [18] and Gekko XII [19], at Institute of Laser Engineering (ILE), Osaka University. A deuterated plastic (CD) target was obliquely irradiated by 1.05 μm laser pulses with the energies of 20–50 J on target and the pulse durations of 450–800 fs using an $f/3.8$ focusing mirror. Both laser systems have intrinsic prepulses that varied in intensity up to 10^{-3} of the main pulse intensity ~700 ps before the main pulse. The maximum intensity of the main pulse was $2\times10^{19}\ \mathrm{W/cm^2}$ from the spot size (~30 μm) obtained from a far field pattern and x-ray pinhole images [19].

Neutron spectra, generated through deuteron-deuteron (D-D) reaction ($d(d,n)^3$He), were observed from several

---

[*] Present address: Central Laser Facility, Rutherford Appleton Laboratory, Chilton, Didcot, Oxfordshire OX11 0QX, UK.

[†] Present address: Lawrence Livermore National Laboratory, P. O. Box 808, 7000 East Avenue, L-399 Livermore, CA 94550, USA.

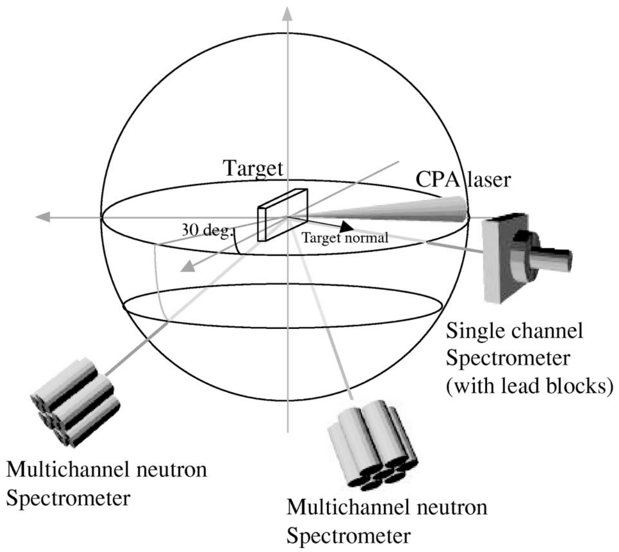

FIG. 1. Typical experimental setup of the detectors for the *p*-polarization condition. The vector angles between detectors and the target normal are 90°, 55°, and 0° from left to right.

viewing angles with neutron spectrometers through the time-of-flight method. Two different types of spectrometers were used in the experiment: The first was a single-channel detector that consisted of a scintillator coupled to a photomultiplier tube to obtain the spectra from the temporal profile of the current output. The second consisted of a 1000-channel detector array to obtain the spectra from a single hit recorded in each channel [20]. Reliable detection ranges of neutron energies of the system were under 15 MeV (single channel) and 20 MeV (multichannel) due to the long trailing edge of the strong γ flash at the laser shot. The energy resolution of the neutron spectra was 29 keV and 100 keV for the multichannel and single-channel detectors, respectively. Figure 1 shows a typical experimental setup for 100 TW laser system. Taking the laser axis as x axis as shown in the figure, the view angles (θ,ϕ) of the detector are $(-42°,0°)$ for single-channel detector $(48°,-30°)$ and $(90°,-30°)$ for multichannel detectors. The distance between the detectors and the interaction point was 3.2 m (single channel) and 13.5 m (multichannel).

All the detectors had a 5 cm-thick cylindrical polyethylene collimator with 5-mm-thick lead blocks inside it to reduce the background noise from γ rays and scattered electrons at the chamber inside, e.g., from the chamber wall and the other diagnostics such as pinhole cameras. Also, in order to reduce the signal level of the γ ray noise directly from the target, 15 cm and 5 cm Pb blocks were placed at the front and the side of the detectors. Neutron scatter effects on the spectra due to the lead blocks were calibrated with thermal neutron signal created in imploded deuterium gas filled in glass microballoon, resulting in the negligible effect to the scattering neutrons in the spectral shape.

III. THREE-DIMENSIONAL MONTE CARLO SIMULATION OF IONS IN SOLID

In general, the shift in the peak of the neutron spectra from the thermonuclear energy in the laboratory frame of reference and the height ratio among the spectra at different viewing angles correspond to the acceleration direction of ions and their energies. On the other hand, the spectral shape reflects the distribution of the accelerated ions, particularly their spatial and temperature distributions. Although single-neutron spectra can be calculated exactly using a knowledge of quantum molecular dynamics when the ion energy exceeds 10 MeV [21], it is difficult to reproduce experimental spectra in laser-plasma interactions analytically because of the large number of fusion reactions occurring at different energies and the probability of ion motion in the solid. In this case, Monte Carlo calculational tools are the most appropriate method to obtain the neutron spectrum generated by nuclear reactions through the propagation of accelerated ions. It is for this reason that a Monte Carlo simulation code was developed to fit the experimental neutron spectra to the calculated spectra, thus providing an initial momentum distribution of the accelerated ions in the three-dimensional momentum space. In the calculation, the target is assumed to be a solid density ($\sim$1.1 g/cm^{-3}) deuterated plastic (polyethylene) plane ($100\times100\times5\ \mu$m^3) with an initial temperature of 0.1 eV (not ionized) and test particle numbers of 8192. The code involves elastic and inelastic interactions described below.

A. Scattering

To calculate multiple scattering in thick targets, the ion angular distribution via small angle scattering by collisions with electrons is given by Jackson's equation [22]:

$$P(\theta)d\theta=\frac{1}{\sqrt{\pi\langle\Theta^2\rangle}}\exp\left(-\frac{\theta^2}{\langle\Theta^2\rangle}d\theta\right). \qquad (1)$$

Here, $\langle\Theta^2\rangle$ is the mean square angle given by

$$\langle\Theta^2\rangle\simeq4\pi N\left(\frac{2zZe^2}{pv}\right)^2\ln(204\ \ Z^{-1/3}t), \qquad (2)$$

where N is the number density, z and Z the charge number of prime and target ions, p and v the momentum and velocity of the prime particle, and t the traverse thickness.

The time step of the calculation is defined to be that required to undergo a sufficient number of collisions in a given cell size in order to maintain the validity of applying these multiple scattering formula.

B. Stopping power

In general, calculations of stopping power in Monte Carlo simulations use Ziegler's semiempirical equations [23,24] for electronic and nuclear stopping power. However, recent studies have shown a threshold effect on the electronic stopping power at low particle energy [25,26] using gases, mainly due to the discontinuity below the minimum excitation energy such as the 1s-2s transition. A similar effect was also reported for stopping powers in insulator targets [27]. In the case studied here, the effect may appear in a few tens keV from the minimum excitation energy of hydrogen (10.198 81 eV : 1s-2s) and carbon (4.182633 eV : 2s-2p)

from the equation $E_{min}=(m_{ion}/zm_e)(1+m_e/m_{ion})^2\ E_{emin}$ [26]. The possibility of a threshold effect occurring was checked in the calculated spectra, but no changes were observed with or without the inclusion of the threshold. This may be due to the fact that the cross section value of D-D reaction at 10 keV is about 10^4 times smaller than the peak at around 1 MeV. However the effect will significantly affect the neutron spectra when deuteron-tritium (D-T) reaction is taken into account where the cross section has a peak around 100 keV.

C. Nuclear reaction

The neutron yield can be represented by

$$Y_n=\int n_{ai}n_{ti}\sigma(v)v\,dt\,dv, \tag{3}$$

where the n_{ai} is the number density of the accelerated ions, n_{ti} the density of the target ions, $\sigma(v)$ the cross section of the nuclear reaction, and v the relative velocity between the accelerated and target ions. Cross sections for the neutron reaction are referred from evaluated and experimental data [28,29].

From the relativistic momentum and energy conservation law, the energy of the neutron at a certain direction in the lab system can be written as

$$E_n=\frac{-(d)\pm\sqrt{(d)^2+4(c)(a)}}{2(c)}, \tag{4}$$

where

$$(a)=2\ \ m_{\rm D}c^2E_{\rm D}-2m_{\rm He}c^2(Q+E_{\rm D})-Q^2-2QE_{\rm D},$$

$$(b)=2(m_nc^2+m_{\rm He}c^2+Q+E_{\rm D}),$$

$$(c)=(4cos^2\theta)(2m_{\rm D}c^2E_{\rm D}+E_{\rm D}^2)-(b)^2,$$

and

$$(d)=(8\cos^2\theta)m_nc^2(2m_{\rm D}c^2E_{\rm D}+E_{\rm D}^2)^2-2(a)(b).$$

Here, $m_{\rm D}$, $m_{\rm He}$, and m_n are the rest mass of deuteron, ^{3}He, and neutron, respectively. Q is the released energy through the nuclear reaction, θ the incident angle, and $E_{\rm D}$ the incident energy of the accelerated deuteron.

D. Examples

Examples of calculated neutron spectra by the Monte Carlo code giving four different momentum distributions are shown in Fig. 2: (a)-1 Isotropic momentum distribution with 100 keV Maxwellian energy distribution (as shown in (a)-2). (a)-3 and (a)-4 show the calculated spectra at target normal and 90° from the normal direction. (b) Anisotropic momentum distribution with 100 keV Maxwellian collimated to target normal direction. The conditions in all the figures are the same as in Fig. 2(a). Figure 2(c) shows the momentum distribution collimated to the target normal direction with constant energy distribution of which the total energy $\int E(\partial N/\partial E)dE$ becomes equal to the 100 keV Maxwellian. Figure 2(d) shows the momentum distribution collimated to 45°. axis from the target normal with a 100 keV Maxwellian energy distribution. By comparing the distributions in (a), (b), and (d), the neutron spectra can be distinguished from each other even though the energy distribution has a similar shape. On the other hand, when the angular distribution is equal, the neutron spectra can be different due to the difference of the energy distribution as shown in (b) and (c). It can be concluded from these results that the ion momentum can be inferred from Monte Carlo fits to the experimental spectra from several viewing angles.

IV. EXPERIMENTAL RESULTS

A. Dependence on the laser incidence

We investigated the momentum distribution of the accelerated ions by changing the laser incidence angle and polarization directions. The solid lines in Figs. 3(a)–3(c) show the experimental neutron spectra at a laser incident angle of 36° to the target normal irradiated by *p*-polarized light with a low prepulse condition (less than 10^{-5}). These spectra are observed at (a) 90°, (b) 55°, and (c) 0° from the front direction of target normal. The signal levels on the figures are normalized to the neutron yield per solid angle, taking into account the detector position and sensitivity. The dashed line across the figures represents 2.45 MeV, the deuteron-deuteron thermonuclear neutron energy. All the experimental spectra show a Doppler shift to the lower energy from 2.45 MeV, which corresponds to the fact that the ions are accelerated into the bulk of the target. Furthermore, the shift increases as the view angle approaches the target normal direction, which suggests that the ion acceleration was anisotropic and directed into the bulk of the target in a collimated flow.

Detailed analysis of the spectra was performed with the three-dimensional (3D) Monte Carlo code to fit the experimental spectra. The dashed lines in Figs. 3(a–c) show that the modeled spectra are well fitted to the experimental results, clearly indicating the collimated ion momentum distribution. For comparison, the spectra corresponding to ions accelerated along the laser axis direction are also shown as the dotted lines. The calculated spectra for the latter case are clearly different from the experimental spectra and also any other energy and momentum distributions. These results rule out that the bulk of ions are accelerated in the direction of the laser incidence.

The fitted three-dimensional momentum distribution is given by an anisotropic Maxwellian distribution. The distribution projected on the x-y plane is shown as a contour plot in Fig. 3(d), where P_x corresponds to the target normal, the P_y corresponds to axis parallel to the target surface, and P_z the direction perpendicular to the figure. Each line represents every $10^{0.4}$ of the ion number in a logarithmic scale. The ion energy in the x direction is about 370 keV whereas the energy in the y as well as in z direction is about 40 keV.

It is interesting to note that the direction of the accelerated ions generated for *s*-polarized light incident onto the target at 20° was in the same direction. Figures 4(a)–4(c) show the neutron spectra for the *s*-polarization condition observed at

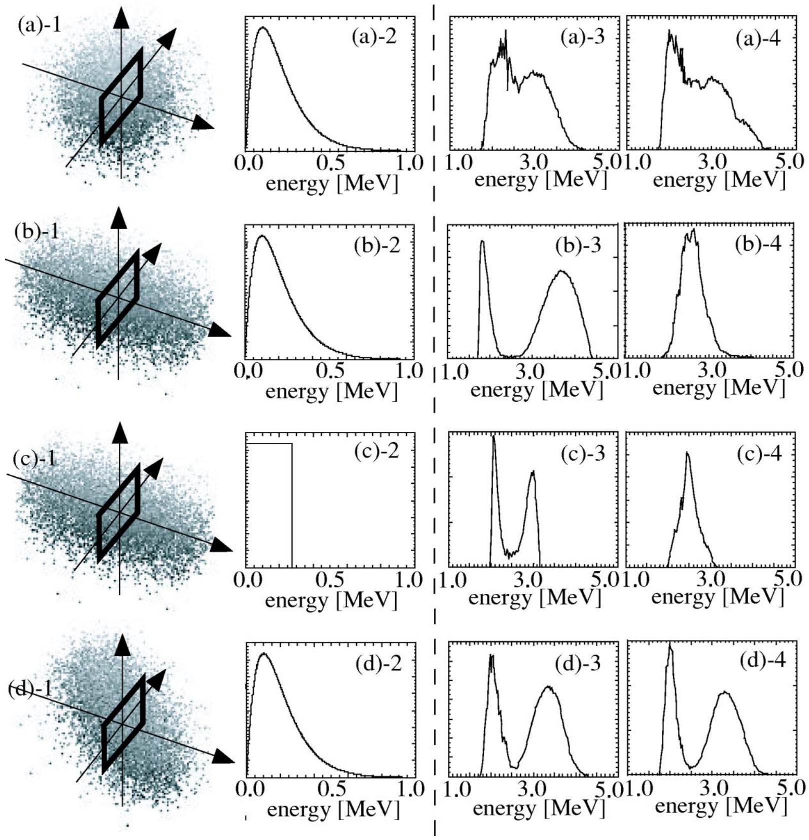

FIG. 2. Examples of deuteron ion momentum distribution and calculated spectra from deuteron-deuteron reaction. The first and second columns show the three-dimensional shape of momentum distribution and extracted energy distribution of ions given in the calculation. The black box in the first column represents the target. The third and fourth columns show the calculated spectra at 0° and 90° from the target normal direction toward the rear. Row (a) indicates an isotropic distribution with Maxwellian energy distribution. (b) Momentum distribution collimated to the target normal direction with Maxwellian energy distribution. (c) Collimated distribution with flat energy distribution. (d) Momentum distribution collimated to 45° from the target normal with Maxwellian distribution.

(a) 88°, (b) 56°, and (c) 35° from the front direction of the target normal. All the conditions in Fig. 4 are same as those of Fig. 3. The neutron spectra also indicate a peak shift to lower energies, which correspond to the ion acceleration into the bulk of the target. The dashed and dotted lines in Figs. 4(a–c) are the calculated spectra giving the initial momentum distribution collimated to the target normal and the laser direction, respectively. The experimental spectra are well fitted with the calculated ones for accelerating along the target normal direction. The momentum distribution is shown in Fig. 4(d) as a contour plot. The momentum distribution is an anisotropic Maxwellian with energies of 330 keV along the x direction and 30 keV along the y and the z direction.

We also studied the momentum distribution of the accelerated ions by changing the incident angles for both laser polarizations. Table I shows the summary of the dependence of the ion acceleration directions on the laser conditions for lower prepulse conditions (less than 10^{-4}). The last column shows the ion energy ratio for each dimensional direction, where E_x corresponds to target normal direction, and E_y, and E_z are the energy to target surface direction. We concluded that the ions are accelerated into the bulk along target normal direction for all incident conditions investigated.

In summary, these results show the ions are accelerated into the bulk along the target normal for all laser incident conditions studied. This indicates that the ions are not accelerated by a direct Coulomb potential between the accelerated electrons and the ions but by static field acceleration (see Appendix).

B. Intensity dependence

We also measured the dependence of the ion acceleration process on the laser intensity. The laser condition was fixed at p polarization 20°. incidence with a low prepulse level ($\ll 10^{-4}$). Figures 5(a) and 5(b) show the neutron spectra observed at 23° and 67° to the rear target normal at 2×10^{18} W/cm^2 and 1×10^{19} W/cm^2, respectively. The signal levels on the spectra are neutron counts per solid angle taking account of the detector sensitivity. The peaks of neutron spectra at the intensity of 10^{18} W/cm^2 were almost exactly at 2.45 MeV as given by the D-D thermal fusion energy. On the other hand, neutron spectra at higher intensity clearly show that the peaks shift to higher energies (2.9 MeV at 23° and 3.0 MeV at 67°). Furthermore, the neutron counts at 1×10^{19} W/cm^2 was larger than the counts at lower intensity and became anisotropic distribution due to the anisotropic

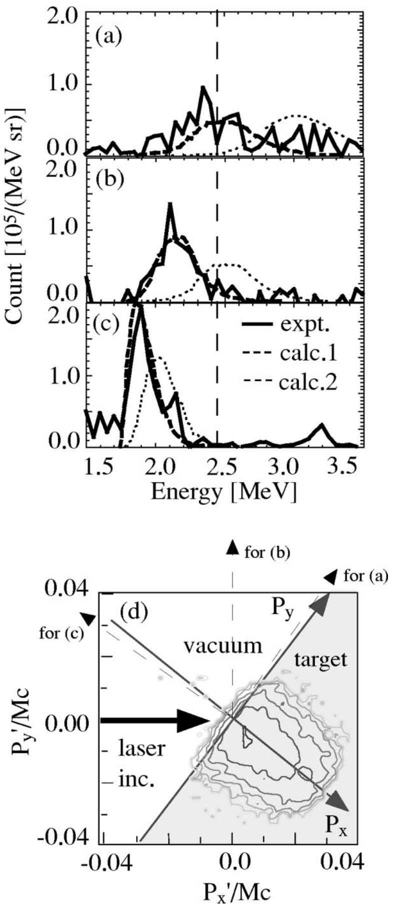

FIG. 3. The neutron spectra for the *p* polarization detected at (a) 90°, (b) 55°, and (c) 0° to the target normal. The solid lines show the experimental results. The dashed and dotted lines show the calculated spectra assuming that the ions are accelerated into the target normal or along the laser direction, respectively. (d) Contour plot of two-dimensional spatial distribution of the ion momentum for the dashed lines in (a)–(c). The momentum is normalized by Mc (M—ion rest mass, c—light speed). Each contour line represents every $10^{0.2}$ of the ion number in a logarithmic scale.

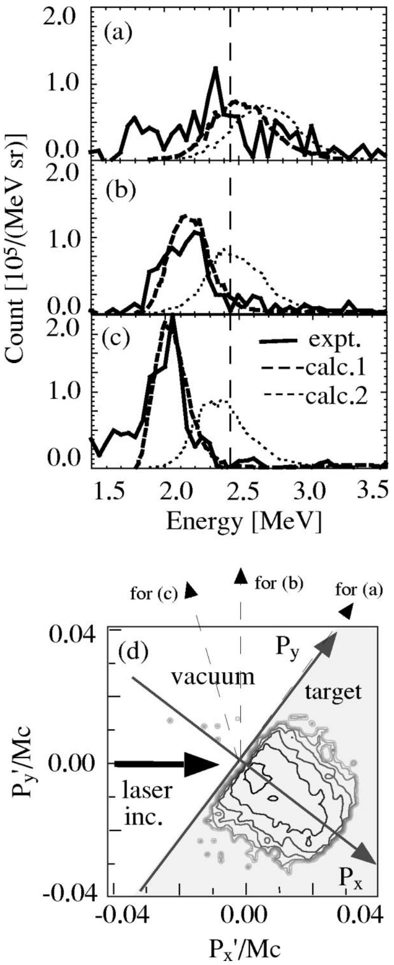

FIG. 4. The neutron spectra for the *s* polarization detected at (a) 88°, (b) 56°, and (c) 35° to the target normal. The experimental spectra are shown by solid lines. The dashed and dotted lines represent the calculated spectra assuming the ion acceleration in the direction of the target normal and in the laser direction, respectively. (d) Contour plot of the two-dimensional distribution of the ion momentum. All other conditions are the same as in Fig. 3(d).

cross section at higher deuteron energy as well as Figs. 3 and 4. These results apparently indicate that higher intensity laser light accelerates the ions to higher energies.

Using the 3D Monte Carlo code, the temperature of the accelerated ion is estimated to be (a) 70 keV and (b) 300 keV by assuming that the ion energy distribution is Maxwellian distributions. The good-fit calculated spectra are also shown in the insets as Figs. 5(a′) and 5(b′). The total number of accelerated ions is similar in both cases and at a few times of 10^{13}, corresponds to a few percent conversion efficiency from the laser energy to energies of ions.

A theoretical picture for the intensity dependence of the ion acceleration process was obtained using particle-in-cell (PIC) simulations. In the simulation code, the deuteron plasma is fully ionized and its geometry has an oblique surface to the laser axis set in the middle of a simulation box (23 μm square). The density profile decreases from $4n_c$ as a maximum density to $0.1n_c$ with a steep exponential shape with a scale length of 0.1 μm. The 1.05 μm laser light with a 200 fs pulse duration irradiates the plasma at an incidence angle of 30° during the simulation time within a 7 μm spot diameter. Figure 6 shows the PIC results for the ion energy distribution at the intensities of 2×10^{18} W/cm^2 (black solid line) and 2×10^{19} W/cm^2 (gray solid line) at *s*-polarization

TABLE I. Dependence of the ion momentum distribution on laser initial conditions. E_x is the ion energy along the target normal direction, whereas E_y and E_z denote the energy along the parallel directions.

Polarization	Incident angle	Accelerated direction	$E_x:E_y:E_z$
p	20°	Target normal	10:1:1
	35°	Target normal	2:1:1
	45°	Target normal	2:1:1
s	20°	Target normal	10:1:1
	45°	Target normal	5:1:1

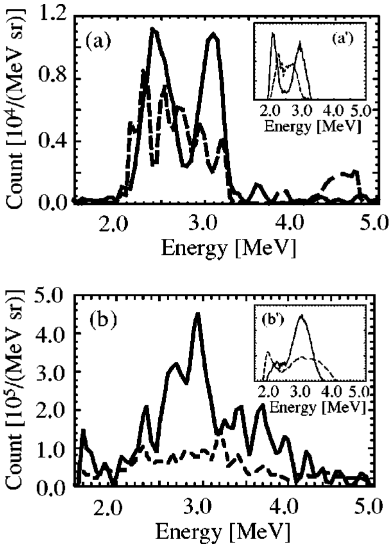

FIG. 5. (a) Neutron spectra for a laser intensity of 2×10^{18} W/cm^2 detected at 23° (solid line) and 67° (dotted line) from the rear target normal. (b) Neutron spectra for a laser intensity of 10^{19} W/cm^2 detected at 23° (solid line) and 67° (dotted line). The good-fit calculated spectra are also shown in the insets as (a′) and (b′).

condition, respectively. In the figure, positive direction on the energy axis corresponds to the target inside and negative to the vacuum side (laser from the left). The ion temperatures corresponding to the target inside and to the vacuum side are 90 keV and 45 keV at 10^{18} W/cm^2, which are almost a quarter smaller than those at the 10^{19} W/cm^2 laser (400 keV for target inside and 120 keV to the vacuum side).

A summary of the experimental results is shown in Fig. 7. Figure 7(a) shows the neutron counts detected at 67° (open circle) and 23° (open square) from rear target normal, corresponding to target front side. All the shots used same target geometry (p polarized 20° incidence and 50-μm-thick CD plane). Neutron counts clearly increased with the laser intensities: the counts at 10^{19} W/cm^2 were about 50 times larger than those at 10^{18} W/cm^2 for both view angles. Because the counts increased linearly in both directions, the angular distribution of the accelerated ion did not appear to change with the laser intensity.

A detailed analysis has also been performed using Monte Carlo fits to the experimental data. The open circles in Fig. 7 (b) indicate the transverse energy of the accelerated ions as estimated by fitting the Monte Carlo calculations to the experimental data. At the same time, the ion energy obtained by PIC simulations is also shown as open triangles in the figure. On the other hand, the open squares show the energy conversion efficiency from the laser to the ions, which were almost constant at a level of 3–8 % for all intensities. This result, the increase of neutron yield is not due to the increase of the number of ions but due to an increased ion energy with increasingly laser intensity, suggests that the ion acceleration depends on the strength of laser field.

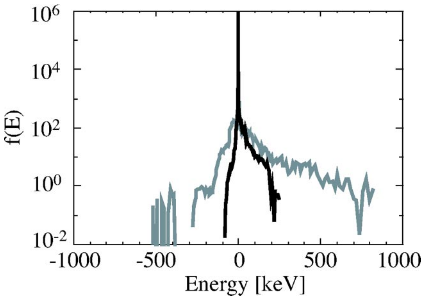

FIG. 6. The ion energy distribution from the PIC simulation results. The black and gray solid lines are the distributions for the intensities of 2×10^{18} W/cm^2 and 2×10^{19} W/cm^2.

The observed laser intensity dependence is well fitted by the computer simulations. To obtain the dependence, a least square fitting was applied to the experimental ion energies. In the results, the ion energy is proportional to $I^{1.04\pm0.2}$ as shown by the dashed line in Fig. 7(b) and follows the well-known dependence of electrostatic field acceleration which is ($u_i \sim I^{1/2}$, then $E_i \sim I$) [12,30]. Considering the results of polarization dependence too, we can conclude that the ion acceleration at the target front is by static field acceleration induced by the accelerated electrons at shorter preplasma scale length.

C. Preplasma dependence

In larger density scale length plasmas, the ion acceleration process might differ from the acceleration process at small scale length interactions. In laser-cluster gas interaction ex-

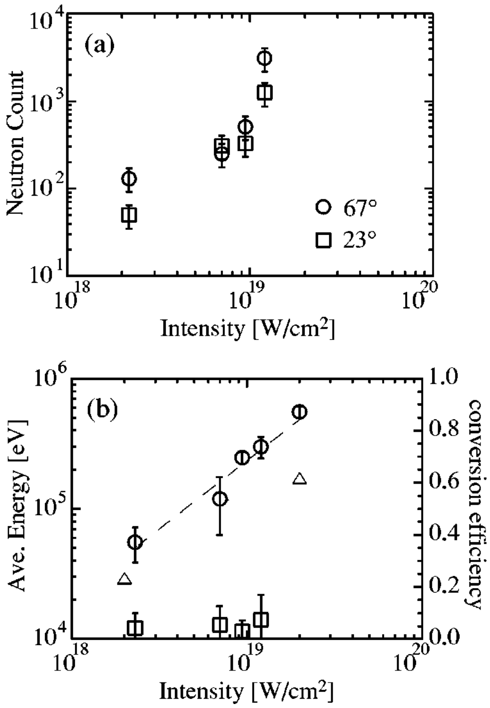

FIG. 7. The intensity dependence of neutron yield and average ion energy. (a) Intensity dependence of neutron yield detected at 67° (circle) and 23° (square) from the rear target normal. (b) The average ion energy from the Monte Carlo fits to the data (open circle) and PIC simulation results (open triangle). The energy conversion efficiency from the laser to the ions is also shown as open squares.

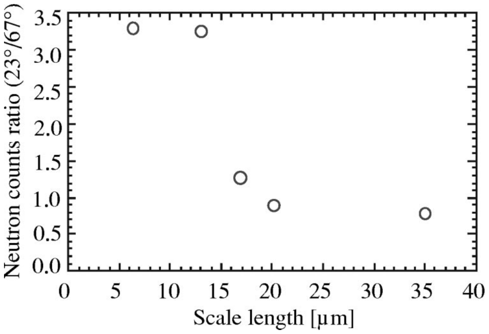

FIG. 8. The dependence of the neutron yield on the estimated scale length of the preformed plasma. The vertical axis represents the ratio of the neutron counts detected at 23° from the rear normal of the target surface divided by the counts at 67°.

periments, it is reported that the ion distribution becomes isotropic due to the Coulomb expansion [8]. The ions can also be expected to accelerate in the longitudinal direction around the laser channel due to the ponderomotive force [30]. To investigate the scale length effect on the ion acceleration, we changed the prepulse levels of the laser by up to 2×10^{-3} of main intensity.

Figure 8 shows the neutron counts ratio for various scale lengths of the preformed plasma. The scale length is calculated by one-dimensional hydrocode [31] from the prepulse intensities. The y axis represents the neutron counts observed at 23° divided by the counts at 67° from target normal direction. As mentioned in the preceding section, in short scale length the neutron counts at the target normal direction are much larger than that at the orthogonal direction because the ion acceleration is collimated to the rear normal direction. However the neutron counts at 23° became even smaller than that at 67° when the scale length was larger than 15 μm. Note the characteristic scale length is almost equivalent with our laser spot radius, and therefore the 1D hydrocode might overestimate the scale length longer than 15 μm due to lack of three-dimensional effect.

This reversion of the neutron counts indicates that the ion acceleration direction indeed changes with plasma scale lengths. Figure 9 shows the neutron spectra and the ion acceleration momentum as the longest scale length of our result as shown in Fig. 8. The solid lines in Figs. 9(a) and 9(b) show the neutron spectra at (a) 23° and (b) 67° from the target normal at an intensity of 6×10^{18} W/cm^2. There were two prepulses at 6.5 ns and 13 ns before the main pulse and the prepulse energies to the main pulse energies were $\sim10^{-3}$. The peak shift to the higher and lower energy side from 2.45 MeV was observed at the side detector, which are shown in Fig. 9(b) (high peak—3.0 MeV, low peak—2.1 MeV). On the other hand, less energy shift were observed at the target normal direction as shown in Fig. 9(a) (high peak—2.9 MeV, low peak—2.3 MeV). The ion acceleration was not collimated to the rear normal of the target surface but parallel to the laser incidence.

The dotted lines in Figs. 9(a) and 9(b) show calculated spectra fitted to the experimental results assuming the ion acceleration perpendicular to the laser incidence direction with a Maxwellian energy distribution. Three-dimensional momentum spatial distributions are given as a momentum ratio of $P_x:P_y:P_z=0.7:1:1$, where P_x corresponds to the target rear side normal, P_y corrsponds to the y axis parallel to the target surface, and P_z is the momentum in the direction perpendicular to the figure. The distribution projected on the x-y plane is shown as a contour plot in Fig. 9(c). Each line represents $10^{0.2}$ of the ion number in a logarithmic scale. The ion number on the x-y plane is integrated along the z coordinate. It is clear that the ion momentum distribution is weakly expanded along the longitudinal direction. The longitudinal ion temperature was about 56 keV. On the other hand, the energy corresponding to the laser incidence was about 28 keV.

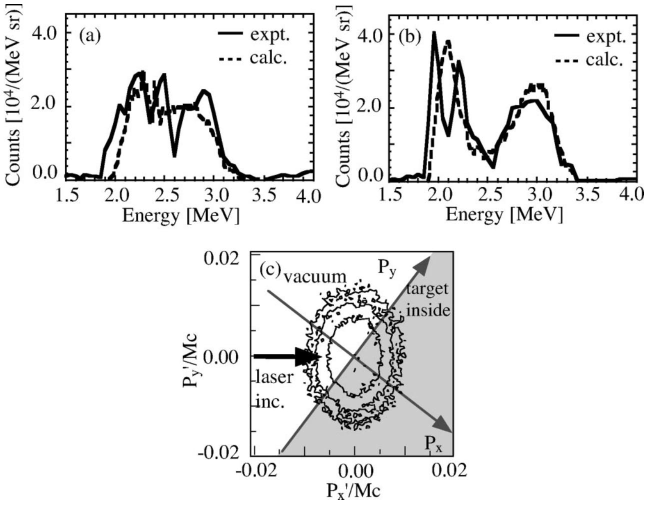

FIG. 9. The neutron spectra for the large scale length detected at (a) 23° and (b) 67° to the target normal. The experimental spectra are shown as black solid lines. The dotted lines represent the well-fitted spectra from the 3D Monte Carlo code assuming the ion acceleration in the direction perpendicular to the laser direction, respectively. (c) Contour plot of two-dimensional spatial distribution of the ion momentum obtained by spectral fitting as shown in (a) and (b). The momentum is normalized to Mc. Each contour line represents $10^{0.2}$ of the ion number in a logarithmic scale.

The result indicates that the ion acceleration in long scale length plasma is different from the acceleration along the target normal direction. The ion acceleration in the longitudinal direction might be due to the laser hole boring [13]. The result is also reasonable by considering that the ion acceleration mechanism is by static potential in the plasma channel along with the deformed wave front, as well as our normal incidence case [11]. However, another ion acceleration so-called ‘‘Coulomb explosion,’’ which is the isotropic ion acceleration by the Coulomb repulsion force among the remaining ions, may also be a candidate for the isotropic acceleration. In the cluster experiment [8,32], over 50 keV Ar^{6+}–Ar^{8+} ions were obtained when the intense laser irradiated the Ar gas with a density of 4.4×10^{21} cm^{-3}. The Coulomb explosion should be proportional to the ion charge, therefore deuteron ions might be impossible to accelerate so high energy and be expected of order of 100 eV.

D. Conclusion

We conclude that the ion acceleration at solid surface is the static field acceleration induced by laser-accelerated hot

TABLE II. Summary of ion acceleration mechanisms.

	Acceleration direction			
Mechanism model	s polarization	p polarization	Intensity dependence of u_i	Plasma length
Direct Coulomb	Laser direction	Target normal	$I^{1/2}$ [a], $I^{5/6}$ [b]	Short scale length
Static field	Target normal	Target normal	$I^{1/2}$	Short scale length
Hole-boring model	Isotropic	Isotropic	$I^{1/2}$	Long scale length
Coulomb expansion	Isotropic	Isotropic		Long scale length
Shock	Laser direction	Target normal	$I^{1/2}$ [c]	Long scale length

[a] Laser duration>(skin depth)/(light speed).

[b] Laser duration<(skin depth)/(light speed).

[c] Only over 10^{18} W/cm^2.

electrons. Whether the hot electrons are accelerated by $J \times B$ heating for s-polarized light or Brunel heating for p-polarized light. A static field is created toward the target normal direction along with the target surface where the electrons are missing. Therefore, the ions on the front surface are always accelerated into the bulk of the target.

As shown in our previous work [17], the ion acceleration can be represented via balance to the laser pressure and the thermal pressure

$$\frac{du_i}{dt} \simeq (1+R)\frac{I}{cl_s} - \frac{n_e k T_e}{L}, \tag{5}$$

where R is the reflection of laser and L the scale length of preformed plasma. When the thermal pressure is smaller than the laser pressure such as low electron temperature due to a small prepulse level or high laser intensity, the ion energy will be proportional to the laser intensity.

We also showed that the ion acceleration clearly changed from anisotropic to isotropic when the scale length exceeds 15 μm which is characterized by the spot radius of our laser system. This isotropic acceleration can be considered as so-called hole-boring model acceleration in the underdense plasma which are already shown in previous works [11].

V. SUMMARY

We measured laser polarization, intensity, and prepulse dependence of neutron spectra to study the ion acceleration mechanism in ultraintense laser interactions with a solid target. Comparing the neutron spectra with the 3D Monte Carlo simulation indicates that the ion acceleration is toward the target normal direction for any laser polarization. We also showed that the ion energy increased in proportion to the laser intensity. These results strongly suggest that the ions are accelerated by a static electric field induced by the charge displacement at the target surface. The prepulse dependence also indicated the static field acceleration of ions along with the deformed laser wave front.

ACKNOWLEDGMENTS

We acknowledge all the technical support of the engineers at Institute of Laser Engineering for the laser operator, target fabrication, and data acquisition. We especially thank Dr. T. Norimatu, Dr. Fujita, Dr. Yoshida, K. Sawai, T. Kawasaki, T. Matsuo, K. Suzuki, Y. Kimura, O. Maekawa, and T. Komenou. We also thank Dr. P. A. Norreys, Rutherford Appleton Laboratory, for useful discussions.

APPENDIX: ION ACCELERATION MECHANISMS

In the appendix, we introduce several mechanisms for ion acceleration reported in recent experimental and simulation results to help to understand our results. Table II shows the short summary of polarization, intensity, and scale length features of these mechanisms. The differences among these mechanisms will help us to identify which ion acceleration is likely to occur.

1. Direct Coulomb acceleration

At a smaller scale length plasma, hot electrons are accelerated along the laser direction by the ponderomotive force. Gamaly estimated the ion energy accelerated by the ponderomotive electrons through the Coulomb potential using a self-similar analysis [12]:

$$\begin{aligned} u_i &\sim I^{1/2}\rho^{-1/2} \quad \text{for} \quad \tau > l_s/c, \\ &\sim I^{5/6}\rho^{-1/2}t \quad \text{for} \quad \tau < l_s/c, \end{aligned} \tag{A1}$$

where I is the laser intensity, ρ the mass density, τ the laser duration, and l_s the skin depth. The boundary value of l_s between two equations $(=\tau c)$ is 140 μm for our laser system, therefore the ion velocity should obey square root of the laser intensity (usually $l_s \ll 1$ μm), resulting in $E_i \propto I$.

Considering the laser interaction with a plane solid target, the acceleration direction of hot electrons is different with the polarization, i.e., laser direction by ponderomotive heating for s polarization and target normal direction due to the resonance and Brunel [33] absorption for p-polarized light. Therefore, the ion acceleration should be different with polarization and plasma scale length.

2. Static field acceleration

At the rear side of solid target, the ions can be accelerated by the static field between escaping electrons and ions. Hatchett indicated the ion energy of the acceleration can be given [9] as

$$E_i = \frac{e|\mathbf{E}|}{m_i} z \propto kT_{hot} \frac{z}{l_{Debye}}, \qquad \text{(A2)}$$

where l_{Debye} is the Debye length representing the acceleration region at the solid rear face, therefore it can be replaced by the skin depth at the target surface. The electron velocity is well known to be proportional to $\sqrt{I}$, therefore the ion energy will also depend on similar relation to the direct Coulomb acceleration.

On the other hand, the acceleration direction can be different from direct Coulomb acceleration mechanism with different laser polarization. The sheath is always generated in front of ions at the target front, therefore the ions should be accelerated to target normal direction at any polarization conditions.

3. Hole-boring model

For longer scale length plasmas, the wave front of intense laser beams become distorted in the underdense plasma and finally generate a plasma channel in the underdense plasma [30]. The ion velocity can be represented by the recession velocity of the wave front, given by

$$\frac{u_i}{c} = \left(\frac{n_c}{2n_{pe}} \frac{Z_i m_e}{M_i} \frac{I\lambda^2}{1.37\times 10^{18}} \right)^{1/2}, \qquad \text{(A3)}$$

where n_c is the critical density, n_{pe} the electron density of the recessing interface, m_e and M_i the electron and ion mass, and I the laser intensity. Then the ion energy will be proportional to the laser intensity again. The direction of ion acceleration should be nearly isotropic or in laser direction which will depend on the wave front shape.

4. Coulomb expansion

In an underdense plasma, the Coulomb expansion of ions is also a possible acceleration mechanism [8]. A resent work shows that deuterons were accelerated up to 100 keV using a cluster as a target [34], the energy which can be sufficient to produce a significant number of neutrons via nuclear reactions. However, unless the target structure is optimized, described in this report, the deuteron energy may be less than a few keV as described in the section of prepulse dependence. The accelerated direction should depend on the charge density of the ions in plasma, therefore the accelerated direction must be isotropic or always symmetric to the target normal axis which will depend on the scale length.

5. Shock acceleration

The ions can be also accelerated by a shock wave at the solid target surface. The maximum ion energy can be characterized by the sound speed of the wave, given by

$$u_i = 2u_s = 2\left(\frac{I}{m_i n_i c}\right)^{1/2}, \qquad \text{(A4)}$$

where u_s is the sound speed. However, Denavit 's calculation [13] indicated the ions might not be able to be accelerated to higher energy when the laser intensity is below 10^{20} W/cm^2.

The shock should be formed along with the direction of hot electron propagation, and therefore the ion acceleration direction must be different from polarization as well as direct Coulomb acceleration.

[1] M. Tabak, J. Hammer, M.E. Glinsky, W.L. Kruer, and S.C. Wilks, Phys. Plasmas **1**, 1626 (1994).

[2] K.W.D. Ledingham *et al.*, Phys. Rev. Lett. **84**, 899 (2000).

[3] D.R. Farley *et al.*, Phys. Rev. Lett. **83**, 1982 (1999).

[4] A.P. Fews, P.A. Norreys, F.N. Beg, A.R. Bell, A.E. Dangor, C.N. Danson, P. Lee, and S.J. Rose, Phys. Rev. Lett. **73**, 1801 (1994).

[5] A. Maksimchuk, S. Gu, K. Flippo, D. Umstadter, and V.Yu. Bychenkov, Phys. Rev. Lett. **84**, 4108 (2000).

[6] K. Krushelnick *et al.*, Phys. Plasmas **7**, 2055 (2000); E.L. Clark *et al.*, Phys. Rev. Lett. **85**, 1654 (2000).

[7] K. Krushelnick *et al.*, Phys. Rev. Lett. **83**, 737 (1999).

[8] T. Ditmire, J. Zweiback, V.P. Yanovsky, T.E. Cowan, G. Hays, and K.B. Wharton, Nature (London) **398**, 489 (1999).

[9] S.P. Hatchett *et al.*, Phys. Plasmas **7**, 2076 (2000); R.A. Snavely *et al.*, Phys. Rev. Lett. **85**, 2945 (2000).

[10] A.J. Mackinnon *et al.*, Phys. Rev. Lett. **88**, 215006 (2002).

[11] N. Izumi *et al.*, Phys. Rev. E **65**, 036413 (2002).

[12] E.G. Gamaly, Phys. Fluids **5**, 3765 (1993).

[13] J. Denavit, Phys. Rev. Lett. **69**, 3052 (1992).

[14] P.A. Norreys *et al.*, Plasma Phys. Controlled Fusion **40**, 175 (1998).

[15] G. Pretzler *et al.*, Phys. Rev. E **58**, 1165 (1998).

[16] L. Disdier *et al.*, Phys. Rev. Lett. **82**, 1454 (1999).

[17] H. Habara *et al.*, Proc. SPIE **3886**, 513 (2000); H. Habara *et al.*, Phys. Plasmas **10**, 3712 (2003).

[18] Y. Kitagawa *et al.*, Fusion Eng. Des. **44**, 261 (1999).

[19] Y. Kato *et al.*, Plasma Phys. Controlled Fusion **39**, A145 (1997).

[20] N. Izumi *et al.*, Rev. Sci. Instrum. **70**, 1221 (1999).

[21] K. Nitta *et al.*, Phys. Rev. C **52**, 2620 (1995).

[22] J. D. Jackson, *Classical Electrodynamics*, 3rd ed. (Wiley, New York, 1998), Chap. 13.

[23] J. F. Ziegler, J. P. Biersack, and U. Littmark, *The Stopping and Range of Ions in Solids* (Pergamon Press, New York, 1985).

[24] H. H. Andersen and J. F. Ziegler, *Hydrogen Stopping Powers and Ranges in All Elements* (Pergamon Press, New York, 1977).

[25] R. Golser and D. Semrad, Phys. Rev. Lett. **66**, 1831 (1991); Nucl. Instrum. Methods Phys. Res. B **69**, 18 (1992).

[26] F. Raiola *et al.*, Eur. Phys. J. A **10**, 487 (2001).

[27] H. Daniel *et al.*, Phys. Lett. A **191**, 155 (1994).

[28] R. J. Howerton *et al.*, *Index to the LLNL Evaluated Charged-Particle Library, Vol. 28* (OECD Nuclear Energy Agency, Moulineaux, France, 1986).

[29] Experimental Nuclear Reaction Data File, Nuclear Data Center, IAEA. http://www-nds.iaea.or.at/exfor/
[30] S.C. Wilks *et al.*, Phys. Rev. Lett. **69**, 1383 (1992); W.L. Kruer and K. Estabrook, Phys. Fluids **28**, 430 (1985).
[31] H. Takabe *et al.*, Phys. Fluids **31**, 2884 (1988).
[32] M. Lezius, S. Dobosz, D. Normand, and M. Schmidt, Phys. Fluids **80**, 261 (1998).
[33] F. Brunel, Phys. Rev. Lett. **59**, 52 (1987).
[34] G. Grillon *et al.*, Phys. Rev. Lett. **89**, 065005 (2002).